Prediction accuracy of Random Forest, XGBoost, LightGBM, and artificial neural network for shear resistance of post-installed anchors

Prediction accuracy of Random Forest, XGBoost, LightGBM, and artificial neural network for shear resistance of post-installed anchors

D. Suenaga[a], Y. Takase[a,*], T. Abe[b], G. Orita[b], and S. Ando[c]

[a] Muroran Institute of Technology, Hokkaido, Japan
[b] Tobishima Corporation, Chiba, Japan
[c] Sumitomo Osaka Cement Co., Ltd., Chiba, Japan
* Corresponding author. E-mail address: y.takase@mmm.muroran-it.ac.jp.

ABSTRACT: Post-installed anchors and reinforcing bars are used to connect equipment or to fasten strengthening members to reinforced concrete (RC) structures. For safety reasons, appropriate structural design is critical. Recently, artificial intelligence (AI) and machine learning (ML) have been applied in various fields. According to previous studies, the bending strength of the RC beam and the bond strength of the surface can be predicted using ML. In this study, the mechanical behavior of post-installed anchors subjected to shear force were predicted using ML. Four algorithms were applied in this study: Random Forest (RF), XGBoost (XB), LightGBM (LG), and an artificial neural network (ANN). Moreover, the authors' previous test results were used for the ML and testing. The number of specimens was thirty-two. The test parameters were the concrete compressive strength f_c, diameter of the anchor bolt d_d, type of adhesive, and tensile ratio r_N. The values for f_c and d_d were set at 13.0-35.5 N/mm^2 and 13-25 mm, respectively. In this study, one epoxy adhesive and three cement-based adhesives were used. r_N, which is the ratio of the tensile stress to yield strength of the anchor bolt, was set to 0, 0.33, and 0.66. Consequently, the four algorithms could accurately predict the mechanical behavior of the specimen when the parameters were within or close to the training data. However, the prediction agreements of RF, XB, and LG were not good for the behavior of specimens whose parameters were not included in the training data. Nevertheless, the ANN was able to reasonably predict the behavior of these cases. It was concluded that the four algorithms can make good predictions when the parameters are within or close to the training data. However, when parameters outside the training data were used, the ANN was the best of the four algorithms used in this study.

Keywords: Post-installed anchor; Post-installed reinforcing bar; Machine learning; Mechanical behavior; Dowel action

1 INTRODUCTION

To connect equipment or to fasten a structural member to existing concrete structures, post-installed anchors or reinforcing bars are used. Design engineering is essential to ensure the safety of the connections. For this reason, methods have been proposed in the design codes [1-5]. In addition, many researchers have investigated the bond properties of post-installed anchors and reinforcing bar. Dowel action was first studied by Friberg [6]. Vintzēleou and Tassios constructed the famous shear strength formula of dowel [7]. Catenary action was introduced to dowel by Sorensen et al. [8] Ghayeb et al. reviewed the dowel joints for precast structures [9]. Alhaidary and Altamimi compared post-installed approved anchor with non-approved anchor [10]. Mahrenholtz et al. presented the design method of post-installed reinforcing bars [11].

Artificial intelligence (AI) or machine learning (ML) are applied to make predictions. Studies on AI have been conducted since the 1950s with the development of computers. As a result, AI and ML have recently been brought back into focus in many fields. For example, ML has been used to predict a default risk of loans [12], daily solar radiation [13], protein-protein interactions [14], and rapid chloride penetration resistance of metakaolin [15]. AI, which includes ML, can help save labor, reduce human error, and provide other benefits.

Many studies have been conducted on the application of AI in concrete structures. For instance, an elastic modulus has been predicted by artificial neural networks (ANN) [16] and support vector machine (SVM) learning [17]. In addition, autogenous shrinkage of concrete has been predicted using ANN [18] and SVM [19]. Kang et al. [20] applied machine learning to predict the compressive and flexural strength of steel fiber-reinforced concrete (SFRC), and concluded that XGBoost and gradient boost re-

gressors could be selected as the most appropriate machine learning methods for predicting these strengths. However, neural networks were not used in this study. In addition, the bond strength between concrete and fiber-reinforced polymers (FRPs) was predicted using ML algorithms, and, it was reported that ML is feasible and efficient for predicting the interfacial bond strength [21]. Olalusi et al. also applied ML to some concrete structures. Using Gaussian process regression (GPR) and support vector regression (SVR), the concrete failure of anchors was predicted [22]. As well, the concrete breakout capacity in shear was predicted by GPR and SVM [23]. Furthermore, the shear capacity of slender RC structures was predicted. [24]

As mentioned earlier, for the safe use of a post-installed anchor or reinforcing bar, structural design is important. For instance, according to ACI-318 [1], the shear strength of anchor is calculated by the following equations.

$$V_{sa} \quad = 0.6A_{se,V}f_{uta}, \tag{1}$$

$$V_b \quad = min\left\{\left(7\left(\frac{l_e}{d_a}\right)^{0.2}\sqrt{d_a}\right)\lambda_a\sqrt{f_c'}(c_{a1})^{1.5}, 9\lambda_a\sqrt{f_c'}(c_{a1})^{1.5}\right\}, \tag{2}$$

where, V_{sa} and V_b are the nominal strength of an anchor in shear and the basic concrete breakout strength, respectively. $A_{se,V}$ is the effective cross-sectional area of an anchor, and f_{uta} is the specified tensile strength of anchor and cannot be taken greater than the smaller $1.9f_y$ and 125 kpsi. f_y is the yield strength of anchor. d_a is the diameter of an anchor, f_c' is the specified concrete compressive strength, c_{a1} is the distance from the center of anchor bolt to the edge of concrete in one direction, l_e is the load bearing length for shear. λ_a is the modification factor for applications in light-weight concrete. In addition, when these are applied to seismic retrofitted structures, consideration of a slip is essential to confirm that the extended members are rigidly connected to the existing members. According to the Japanese guideline [5], Q_a, which is the shear

strength formula with considering a slip, is used as per the following equations.

$$Q_a = \psi \cdot min\left(0.7 f_y, 0.4\sqrt{E_s \cdot f_c}\right) \cdot A_s, \tag{3}$$

where, E_s and f_c are Young's modulus of anchor and compressive strength of concrete, respectively. A_s is the cross-sectional area of anchor. ψ is the coefficient for considering a slip; $\psi = 0.7$ is applied. For the structural design with considering the slip, estimating the dowel action is important; thus, a mechanical model is useful. Hence, the authors studied the mechanical behavior of post-installed dowel bars. As mentioned above, ML was applied to concrete engineering; however, prediction methods for dowel action were not studied. Therefore, in this study, the authors proposed a new prediction method with ML. By using the authors' previous test results of post-installed anchors [26-28], the prediction accuracies of the four ML algorithms, which are named Random Forest, XGBoost, LightGBM, and an artificial neural network, were investigated. The objective of this study is to investigate whether the dowel action can be predicted by ML. The prediction accuracy of the four algorithms was also considered. Section 1 describes the introduction and motivation, Section 2 provides the details of the test, Section 3 explains the details of ML, which were used in this study, and, Section 4 presents the results of the test and training accuracy. Finally, Section 5 discusses the prediction accuracy and Section 6 provides the conclusions.

Nomenclature

A_s: cross-section area of dowel bar (mm^2) [32]

$A_{se,V}$: effective cross-sectional area of an anchor (in.^{2}) [1]

c_{a1}: distance from the center of an anchor shaft to the edge of concrete in one direction (in.) [1]

E_c: Young's modulus of concrete (N/mm^2)

E_g: Young's modulus of grout (N/mm^2)

E_s: Young's modulus of dowel bar (N/mm^2)

f_c: cylinder compressive strength of concrete (N/mm^2)

$f_c{'}$: specified compressive strength of concrete (psi)

f_g: cylinder compressive strength of grout (N/mm^2)

f_{gt}: tensile strength of grout (N/mm^2)

f_y: yield strength of anchor (N/mm^2 or psi)

f_t: tensile strength of concrete (N/mm^2)

f_{uta}: specified tensile strength of anchor (psi) [1]

$k(x, x')$: Kernel function

l: hyper parameter of Eq. (5)

l_e: load bearing length of anchor for shear (in) [1]

L_e: embedded length of dowel bar (in) [1]

MAE: mean absolute error

$m(x)$: mean function

R^2: coefficient of determination

$RMSE$: root mean squared error

r_φ: φ/d_d

Q: shear force in the test (N)

Q_a: shear strength of anchor (N) [5]

Q_{ana}: shear force of the analytical results (N)

Q_d: shear strength of dowel bar calculated by the previous model (N) [25-27]

Q_{max}: maximum shear force in the test (N)

r_N: tensile ratio

V_b: concrete breakout strength of an anchor (lb) [1]

V_{sa}: nominal strength of an anchor (lb) [1]

y_i: test value of the number i

$\hat{y}_i$: prediction value of the number i

$\bar{y}_i$: average value of y_i

δ: shear displacement (mm)

δ_{max}: shear displacement at Q_{max} (mm)

λ_a: modification factor for applications in light-weight concrete [1]

ρ_l: ratio of longitudinal bar (%)

ρ_t: ratio of transverse bar (%)

σ_f: hyper parameter of Eq. (5)

τ_a: bond strength of adhesive (N/mm^2)

φ: diameter of drilling hole (mm)

ψ: coefficient for considering a slip [5]

2 DETAILS OF SHEAR LOADING TEST

In this section, the details of the shear loading test are presented. The specimen shape and loading setup were the same as in previous studies [26-28]; although new three test parameters were added. Therefore, the specimen parameters are described in detail in this section; and, the loading method is briefly explained.

2.1 *Test parameters*

Table 1 lists the specimen parameters and the material properties of the dowel bars, concrete, grout, and adhesives. The Japanese Industrial Standard [30-32] was applied for the material tests.

The test parameters of the specimens were the type of adhesive, the diameter of anchor bolt d_d and, the drilling hole φ, the concrete cylinder compressive strength f_c, and the tensile ratio r_N. Here, r_N is the ratio of the applied tensile stress to f_y.

In this study, four types of adhesives were used: epoxy adhesive Ep, normal cement-based adhesive Ce, winter-type cement-based adhesive CeW, and fluidization-type cement-based adhesive CfW. The water to cement ratio of Ce was 20.3 %. Ce is the Japan Construction Anchor Association (JCAA [29])-approved anchor, whereas Ep is a European technical assessment (ETA)-approved anchor [3]. In CeW, lithium nitrite ($LiNO_3$) was added to Ce. The consistency of $LiNO_3$ in the water was 14.3 %. Additionally, in CfW, half the size of the compound was used compared to Ce to improve fluidization for good workability. The r_N was set to 0, 0.33, and 0.66, as in previous tests [26-28], d_d was set to 13, 16, 19, 22, and 25 mm, and f_c was set to 13.0–35.5 N/mm².

Table 1
Parameters of the shear loading test. The numerical values of the specimen ID indicate d_d (φ), f_c, and r_N, respectively. E_s (N/mm²) is Young's modulus of the anchor bolt. E_c (N/mm²) and f_t (N/mm²) are Young's modulus and the tensile strength of concrete, respectively. f_g (N/mm²), E_g (N/mm²), and f_{gt} (N/mm²) are the cylinder compressive strength, Young's modulus, and tensile strength of grout, respectively. τ_a (N/mm²) is the bond strength of adhesive. Specimens with a check mark in the "Train. data set" column were used for training data for ML.

Specimen ID	Dowel bar					Concrete			Grout			Adhesive	r_N	Train. data set
	d_d	A_s	φ	f_y	E_s	f_c	E_c	f_t	f_g	E_g	f_{gt}	τ_a		
Ep-D16(22)-26.1-000 [26,27]	16	198.6	22	376	174	26.1	18.4	1.9	67.3	25.2	3.3	30.2	0.00	✓
Ep-D16(22)-26.1-033 [26]	16	198.6	22	376	174	26.1	18.4	1.9	67.3	25.2	3.3	30.2	0.33	✓
Ep-D16(22)-26.1-066 [26]	16	198.6	22	376	174	26.1	18.4	1.9	67.3	25.2	3.3	30.2	0.66	
Ep-D16(22)-20.9-000 [26]	16	198.6	22	387	175	20.9	24.6	1.9	72.0	27.5	3.1	22.6	0.00	✓
Ep-D16(28)-20.9-000 [26]	16	198.6	28	387	175	20.9	24.6	1.9	72.0	27.5	3.1	24.1	0.00	✓
Ep-D16(32)-20.9-000 [26]	16	198.6	32	387	175	20.9	24.6	1.9	72.0	27.5	3.1	27.0	0.00	✓
Ep-D16(22)-35.5-000	16	198.6	22	387	175	35.5	27.0	2.9	69.1	27.4	2.8	26.2	0.00	✓
Ep-D13(16)-35.5-000	13	126.7	16	385	171	35.5	27.0	2.9	69.1	27.4	2.8	23.8	0.00	✓
Ep-D19(24)-35.5-000	19	286.5	24	393	176	35.5	27.0	2.9	69.1	27.4	2.8	25.7	0.00	✓
Ce-D16(20)-13.0-000 [26-28]	16	198.6	20	403	173	13.0	15.6	1.0	63.6	26.5	2.9	20.3	0.00	✓
Ce-D16(20)-13.0-033 [26-28]	16	198.6	20	403	173	13.0	15.6	1.0	63.6	26.5	2.9	20.3	0.33	✓
Ce-D16(20)-24.8-000 [26-28]	16	198.6	20	403	173	24.8	18.2	1.6	63.6	26.5	2.9	20.3	0.00	✓

Ce-D16(20)-24.8-033 [26-28]	16	198.6	20	403	173	24.8	18.2	1.6	63.6	26.5	2.9	20.3	0.33	✓
Ce-D16(20)-24.8-066 [26-28]	16	198.6	20	403	173	24.8	18.2	1.6	63.6	26.5	2.9	20.3	0.66	✓
CeW-D16(20)-13.0-000 [27,28]	16	198.6	20	403	173	13.0	15.6	1.0	63.6	26.5	2.9	20.2	0.00	✓
CeW-D16(20)-13.0-033 [27,28]	16	198.6	20	403	173	13.0	15.6	1.0	63.6	26.5	2.9	20.2	0.33	✓
CeW-D16(20)-13.0-066 [27,28]	16	198.6	20	403	173	13.0	15.6	1.0	63.6	26.5	2.9	20.2	0.66	✓
CeW-D16(20)-24.8-000 [27,28]	16	198.6	20	403	173	24.8	18.2	1.6	63.6	26.5	2.9	20.2	0.00	✓
CeW-D16(20)-24.8-033 [27,28]	16	198.6	20	403	173	24.8	18.2	1.6	63.6	26.5	2.9	20.2	0.33	✓
CeW-D16(20)-24.8-066 [27,28]	16	198.6	20	403	173	24.8	18.2	1.6	63.6	26.5	2.9	20.2	0.66	✓
CeW-D16(20)-25.1-000 [27,28]	16	198.6	20	387	175	25.1	21.1	2.3	68.6	27.4	2.8	21.0	0.00	✓
CeW-D22(28)-25.1-000 [27,28]	22	387.1	28	409	180	25.1	21.1	2.3	68.6	27.4	2.8	17.3	0.00	✓
CeW-D22(32)-25.1-000 [27,28]	22	387.1	32	409	180	25.1	21.1	2.3	68.6	27.4	2.8	19.5	0.00	✓
CeW-D25(32)-25.1-000 [27,28]	25	507.6	32	426	210	25.1	21.1	2.3	68.6	27.4	2.8	17.0	0.00	✓
CfW-D16(20)-25.1-000-1 [28]	16	198.6	20	387	175	25.1	21.1	2.3	68.6	27.4	2.8	19.8	0.00	✓
CfW-D19(24)-25.1-000 [28]	19	286.5	24	434	190	25.1	21.1	2.3	68.6	27.4	2.8	18.8	0.00	
CfW-D22(28)-25.1-000 [28]	22	387.1	28	409	180	25.1	21.1	2.3	68.6	27.4	2.8	17.8	0.00	✓
CfW-D25(32)-25.1-000 [28]	25	507.6	32	426	210	25.1	21.1	2.3	68.6	27.4	2.8	16.8	0.00	✓
CfW-D16(20)-25.1-000-2 [28]	16	198.6	20	387	175	25.1	21.1	2.3	70.0	26.4	3.9	19.8	0.00	✓
CfW-D16(20)-25.1-033 [28]	16	198.6	20	387	175	25.1	21.1	2.3	70.0	26.4	3.9	19.8	0.33	✓
CfW-D16(20)-25.1-066 [28]	16	198.6	20	387	175	25.1	21.1	2.3	70.0	26.4	3.9	19.8	0.66	✓
CfW-D16(28)-25.1-000 [28]	16	198.6	28	387	175	25.1	21.1	2.3	70.0	26.4	3.9	19.8	0.00	

2.2 Shear loading test

2.2.1 Details of the specimens

Fig. 1 shows the details of the specimen [26,27]. The specimen consisted of concrete and grout blocks. The dimensions of the concrete and grout block specimens were 440 mm × 460 mm × 250 mm and 375 mm × 200 mm × 190 mm, respectively. Since the concrete was cast vertically, the surfaces of the joint sides had a smooth finish with plywood as the formwork. In addition, the surface was greased; thus, the friction on the surface was insignificant. The ratios of the longitudinal bar p_l and the transverse bar p_t in the concrete block were 0.74 % and 0.28 %, respectively, whereas the ratios of the grout block were 0.75 % and 0.76 %, respectively. After the concrete block was air-dried for 28 d, a hole was bored at the center of the top of the block using a diamond core drill. Subsequently, the dowel bar was adhered using an epoxy or cement-based adhesives. After adhering dowel bar, the reinforcing bars and the formwork of the grout block were set. The premixed cementitious grout was then cast. After 14 d, the formworks were removed; moreover, after more 14 d of moist curing, the specimens were tested.
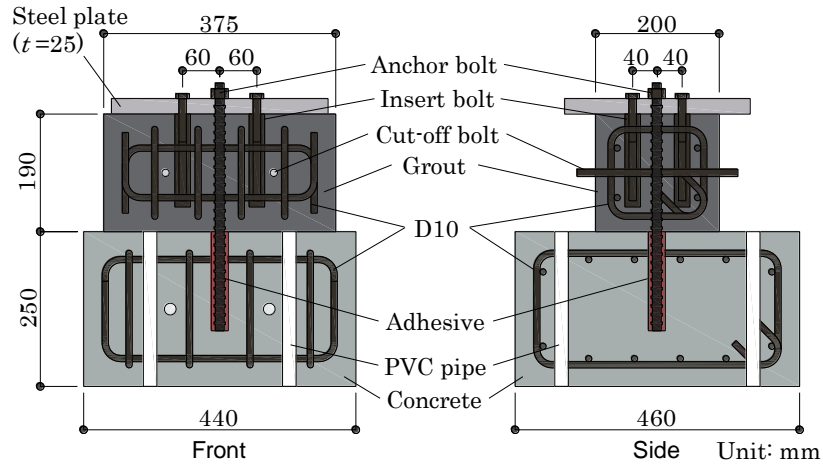
Fig. 1 Characteristics of specimens for shear loading tests. The embedded length L_e was $10d_d$.

2.2.2 *Loading and measurement setup*

Figs. 2 and 3 show the loading setup and the measurement setup for displacement, respectively, which are the same as those used in previous tests [26,27]. In the loading setup shown in **Fig. 2**, two 150 kN screw jacks and a 500 kN hydraulic jack were used. By controlling the two screw jacks, the loading beams moved parallel to the surface during shear loading. A static cyclic shear load was applied to the specimen at a loading rate of 0.02–0.04 mm/s. The loading cycle was ±0.25, ±0.50, ±1.0, ±1.5, ±2.0, ±3.0, ±4.0, ±6.0, and ±8.0 mm. During shear loading, the surface was moved horizontally and vertically; therefore, the slip δ and the opening of the surface were measured using the four displacement sensors shown in **Fig. 3**.

8

(a) Front view.

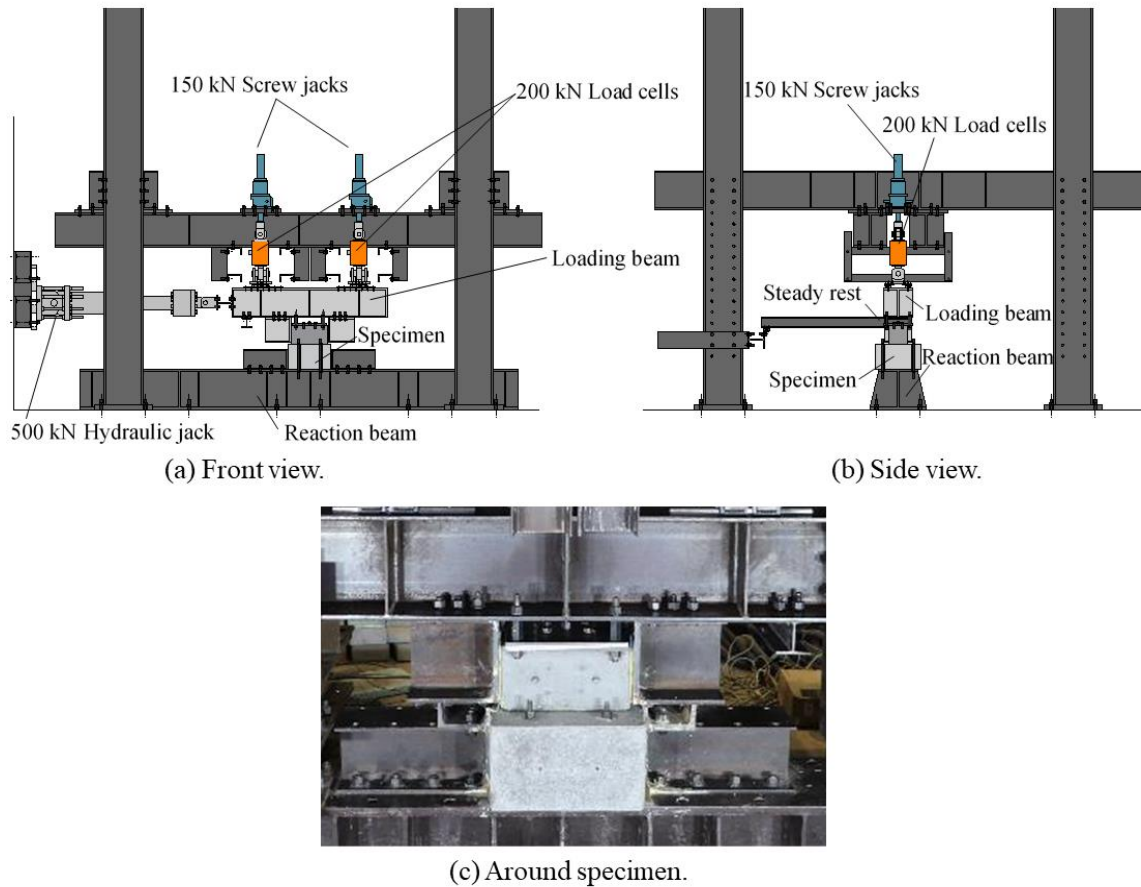(b) Side view.

(c) Around specimen.

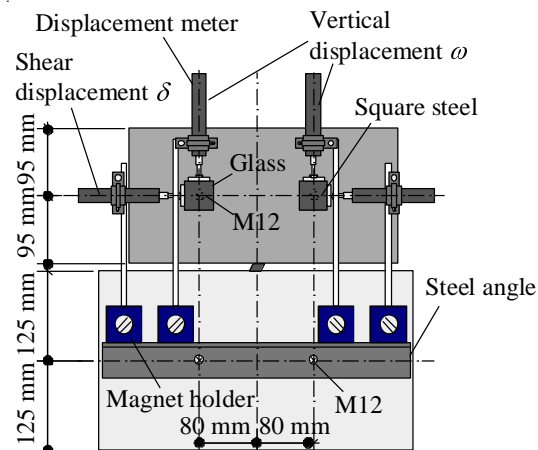Fig. 2 Loading setup for the shear loading test [26].

Fig. 3 Setup for measuring displacement [26].

2.3 *Bond-slip test*

Although the training data are explained in Section 3.6, the bond strength was used

for the training data. Therefore, in this section, the outlines of bond-slip test are briefly

explained. The maximum bond stresses, τ_a, are listed in **Table 1**.

Fig. 4 shows the outlines for the bond-slip test. [26] The specimen parameters and

manufacturing procedures were the same as those in the shear loading test. Moreover, the bond-slip test was performed at the same time as the shear loading tests. The specimens were rectangular; and fifteen anchor bolts were adhered to each specimen. To investigate the bond strength, L_e was set to 4.5 d_a; and, to prevent concrete cone failure, a reaction plate was used. Tensile force was applied using a 320 kN hydraulic center-hole jack; then, the tensile force was applied manually at a loading rate of 0.005–0.02 mm/s. A monotonic tensile force was applied to the anchors.
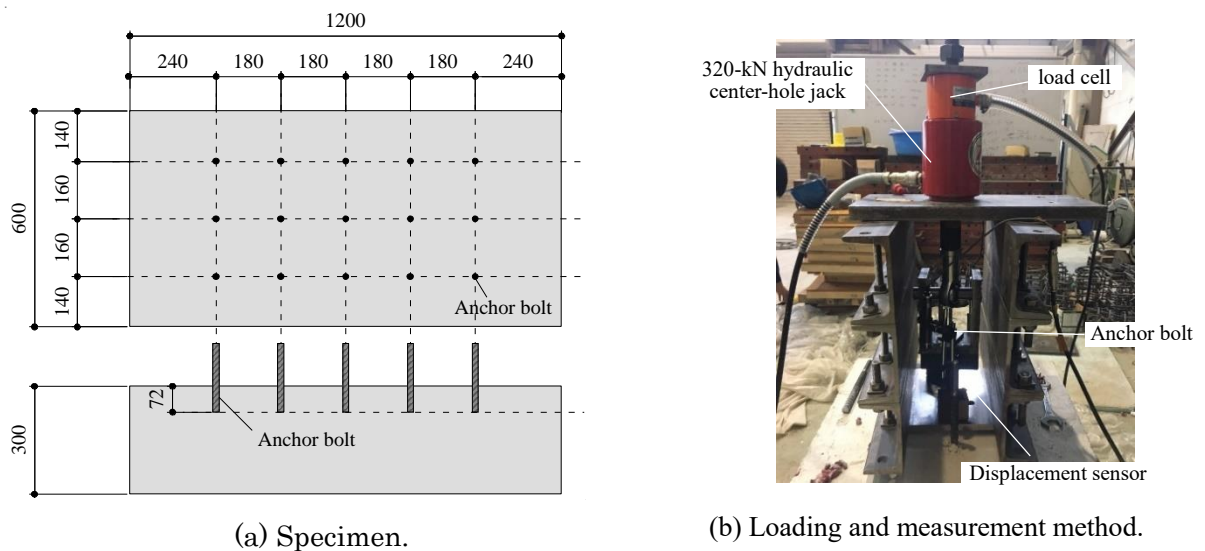

(a) Specimen.   (b) Loading and measurement method.

Fig.4 Outlines of bond-slip tests. [26]

3 OUTLINES OF MACHINE LEARNING APLLIED IN THIS STUDY

Fig. 5 shows an image of the machine learning models used in this study. As shown in **Fig. 5**, four types of machine learning were used, Random Forest (RF), XGBoost (XB), LightGBM (LG), and an ANN. RF, XB, and LG are categorized by the type of decision tree. Whereas, the structure of the ANN is similar to that of the human brain. This section provides an overview of the machine learning used in this study.
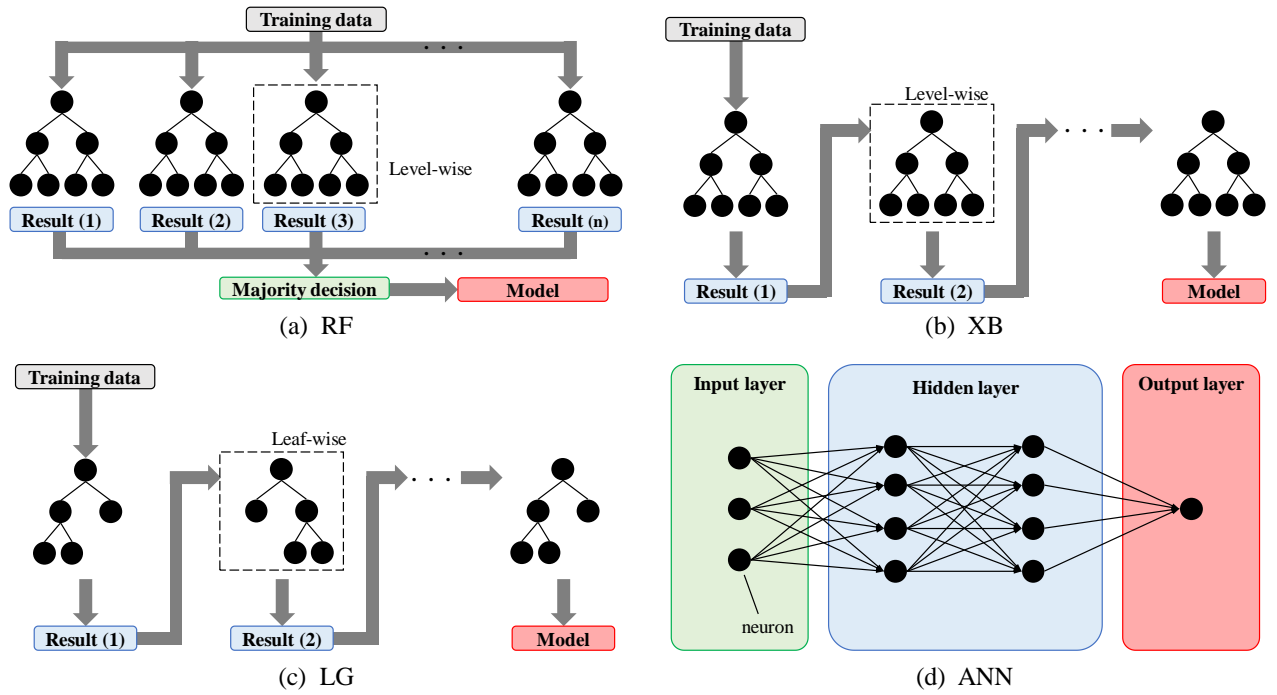
Fig. 5 Image of the machine learning used in this study.

3.1 *Random Forest*

RF was proposed by Breiman in 2001 [33] and is a learning model based on a decision tree. An ensemble learning is applied to RF. For this reason, overfitting is a major problem in ML; therefore, to solve this problem, many decision trees are constructed in parallel in RF, as shown **in Fig. 5** (a). Moreover, in ensemble learning, "bootstrap aggregation" is applied so that the same data can be repeatedly used for many decision trees. The prediction results are then determined by a majority decision. This improved the prediction accuracy.

3.2 *XGBoost (eXtream Gradient Boosting)*

In RF, many decision trees are built using bootstrap aggregation. Gradient boosting and decision trees (GBDT) are also popular algorithms for ML. XB was proposed by Chen and Guestrin in 2016 [34]. XB is based on the GBDT; thus, when multiple decision trees are constructed, weighting coefficients for weak classification are applied to the next decision tree so that the loss is gradually reduced. There are two types of

trees: classification and regression trees. In this study, a regression tree was used.

For the decision tree, the level-wise tree method is applied; therefore, the decision tree grows with each layer. Moreover, based on the GBDT, the final outputs are determined by the average of the outputs of several trees. XB has been used in several studies [12,15].

3.3 *LightGBM (Light Gradient Boosting Machine)*

LG is also based on GBDT as well as XB. In general, the larger the number of training data, the lower are the efficiency and accuracy. To solve this problem, gradient-based one-side sampling (GOSS) and exclusive feature bundling (EFB) were applied to the LG. Large datasets can be used by GOSS. Moreover, many data features are managed by EFB. In addition, the leaf-wise tree is applied; i.e., the decision trees grow with each leaf, as shown in **Fig. 5** (c). Based on these techniques, it was reported that the learning time was 20 times shorter than that of the conventional GBDT algorithm with the same accuracy [35].

3.4 *Artificial Neural Network*

An ANN is a mathematical model that resembles the human brain and consists of an input layer, hidden layer, and an output layer. There are neurons in each layer; moreover, one neuron is connected to the next neuron by convolutions. In this study, the number of input layer nodes was eight, similar to the input items described in Section 3.6, and the number of hidden layers was two. In addition, the layers had 64 and 32 nodes. The number of nodes for the output layers was one, which represented the shear load. Furthermore, a normalized linear function is used for effective learning.

3.5 *Other algorithms*

As mentioned in Section 1, SVM, SVR, and GPR were also used in the previous studies; moreover, it was reported that these algorithms were applicable to predict the strengths of RC structures. In SVM and SVR, response variables are classified into two groups by a support vector, and a linear or polynomial Kernel functions are employed. Whereas, in GPR, Kernel function is based on Gaussian distribution. For instance, the following equations are used.

$$f(x) \sim GP(m(x), k(x, x')), \tag{4}$$

$$k(x, x') = \sigma_f^2 exp\left(-\frac{(x - x')^2}{2l^2}\right), \tag{5}$$

where, *GP* is Gaussian process, *m(x)* is the mean function, σ_f and *l* are the hyper parameters. Generally, applying these algorithms to high dimension and large-scale data sets is difficult because a matrix size of Kernel function is $n \times n$; where, *n* is the number of a data set. Therefore, in the previous studies, these algorithms were used for predicting a simple response variable such a strength. In other words, these were not applied to complicated variables. Whereas, the load – defection curves of RC beam were predicted using ANN [36]. Hence, in this study, RF, XB, LG, and ANN, which can predict complicated phenomena, were employed.

3.6 *Training data set*

In this study, Python 3.8 was used for ML. **Table 2** lists an example of training data. In this study, *Q* is the response value and f_c, f_g, A_s, r_φ, f_y, τ_a, r_N, and δ are the training data. Here, $r_\varphi = \varphi / d_d$. The value of A_s was determined based on the Japanese standard [32]. These values were extracted from all the test data and summarized in a CSV file, as shown in **Table 2**. The number of lines in the test data was 7,950. 80 % of the training data was randomly selected and then used for learning. The remaining 20 % was

used to test the training accuracy. As shown in **Table 1**, the number of the specimens with d_d = 16 mm is 22 out of 32; therefore, the balance of d_d is not good. However, RF, XB, LG, and ANN can predict the objective variables with each training item separated. Hence, in this study, the specimens with various d_d were used for the data set.

Table 2
Example of the training data.

f_c	f_g	A_s	r_φ	f_y	τ_a	r_N	δ	Q
26.1	67.3	198.6	1.375	376	30.2	0.00	0.000436	1.591754
26.1	67.3	198.6	1.375	376	30.2	0.00	0.000799	1.846615
26.1	67.3	198.6	1.375	376	30.2	0.00	0.002047	2.133334
26.1	67.3	198.6	1.375	376	30.2	0.00	0.003540	2.451910
|	|	|	|	|	|	|	|	|
25.1	70.0	198.6	1.25	387	19.8	0.66	7.975880	23.07971
25.1	70.0	198.6	1.25	387	19.8	0.66	8.014048	22.84077

Table 3 lists an example of the validation and prediction data. In these data, the training items were selected; however, Q was removed because it was predicted. The values of δ for the test results were random, as listed in **Table 2**. However, random data are not known for prediction. Therefore, regular values were used as δ, as shown in **Table 3**.

Table 3
Example of the data used for validation and prediction.

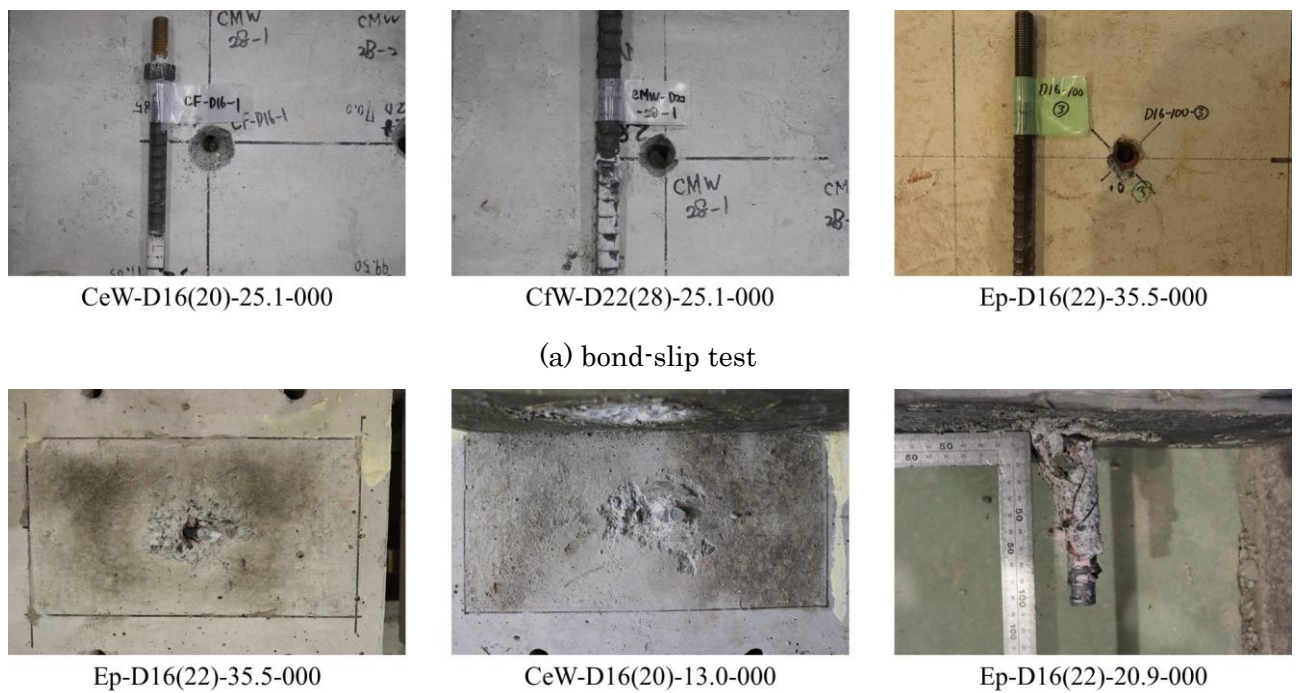| f_c	f_g	A_s	r_φ	f_y	τ_a	r_N	δ
26.1	67.3	198.6	1.375	375.8	30.2	0.66	0.00
26.1	67.3	198.6	1.375	375.8	30.2	0.66	0.01
26.1	67.3	198.6	1.375	375.8	30.2	0.66	0.02
26.1	67.3	198.6	1.375	375.8	30.2	0.66	0.03
|	|	|	|	|	|	|	|
26.1	67.3	198.6	1.375	375.8	30.2	0.66	7.99
26.1	67.3	198.6	1.375	375.8	30.2	0.66	8.00

4 TEST RESULTS AND TRAINING ACCURACY

4.1 *Loading test results*

4.1.1 *Failure mode*

Figs. 6 (a) and (b) show the failure modes for the bond-slip and shear loading tests, respectively.

As shown in **Fig. 6** (a), the anchors failed at the surface between the anchor bolt and the adhesive. Concrete breaks were observed around the hole, but no cracks were observed. Therefore, it can be concluded that the main failure mode was bond failure. Subsequently, **Fig. 6** (b) focuses on the shear loading test. Although a small concrete fracture was confirmed around the hole due to bearing stress, no noticeable cracks were observed on the concrete surface. Therefore, based on the test results, a pure dowel action could be considered.

| CeW-D16(20)-25.1-000 | CfW-D22(28)-25.1-000 | Ep-D16(22)-35.5-000 |

(a) bond-slip test

| Ep-D16(22)-35.5-000 | CeW-D16(20)-13.0-000 | Ep-D16(22)-20.9-000 |

(b) shear loading test
Fig.6 Failure modes of the test.

4.1.2 *Maximum shear load*

Table 4 lists the test results for all specimens. The validation results, which are explained in Section 5.1, are also listed in **Table 4**. For the dowel action of the post-installed anchors, the shear force Q increases with increasing δ. Moreover, for the safe use of post-installed anchors, the shear displacement should be small during the design strength. Therefore, the behavior up to $\delta = 8$ mm was used for the investigation in this test. Due to this condition, Q_{max} was the maximum shear load up to $\delta = 8$ mm

in this study. δ_{max} denotes the shear displacement at Q_{max}.

Table 4 shows that for some specimens, namely Ep-D16(32)-20.9-000, Ce-D16(20)-24.8-033, and CeW-D16(20)-13.0-033, the δ_{max} value is small, approximately 1 mm. In contrast, for Ep-D16(22)-20.9-000, Ce-D16(20)-13.0-000, CeW-D16(20)-13.0-066, CeW-D22(32)-25.1-000, and CfW-D16(20)-25.1-000-1 to CfW-D25(32)-25.1-000, the δ_{max} value is large, approximately 8 mm, therefore, Q increases after δ = 8 mm. Except for these specimens, the values of δ_{max} are in the range of 2–6 mm.

Subsequently, **Fig. 7** examines the relationship between Q_{max} and test parameters. To normalize, the ratio r_φ between φ and d_d is used. As shown in **Fig. 7**, as f_c and r_φ increase, Q_{max} increases. As r_N increases, Q_{max} decreases. According to the Q_{max}–r_N relationships, Q_{max} was smaller for the cement-based anchors than for the epoxy adhesive anchors. These features were mentioned in a previous study [26-28].
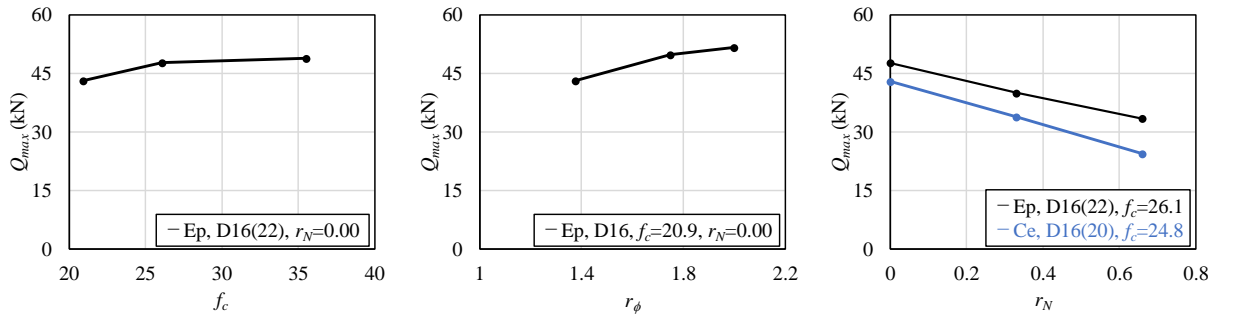

Fig.7 Relationship between Q_{max} and the parameters.

Table 4
Test and validation results. δ_{max} is the shear displacement during Q_{max}.

Specimen ID	Pred.	Test		RF		XB		LG		ANN	
		Q_{max}	δ_{max}	Q_{max}	δ_{max}	Q_{max}	δ_{max}	Q_{max}	δ_{max}	Q_{max}	δ_{max}
Ep-D16(22)-26.1-000	A	47.72	6.01	47.34	5.82	48.33	5.91	48.67	5.96	46.36	8.00
Ep-D16(22)-26.1-033	A	40.02	5.92	39.76	5.81	40.08	5.86	40.62	5.96	39.28	5.77
Ep-D16(22)-26.1-066	B	33.43	3.07	36.87	5.89	30.82	5.91	30.80	5.96	34.66	5.83
Ep-D16(22)-20.9-000	A	43.17	8.00	43.03	7.95	43.23	7.97	43.18	8.00	43.18	8.00
Ep-D16(28)-20.9-000	A	49.90	1.91	49.71	1.91	49.82	1.89	49.82	1.96	49.39	1.67
Ep-D16(32)-20.9-000	A	51.73	1.01	51.27	0.98	51.53	1.00	52.18	0.99	51.13	1.34
Ep-D16(22)-35.5-000	A	48.87	5.93	48.78	5.91	48.84	5.91	48.75	5.86	48.07	5.83
Ep-D13(16)-35.5-000	A	34.72	5.15	34.24	5.15	34.51	5.98	34.20	5.96	33.59	3.45
Ep-D19(24)-35.5-000	A	70.23	5.88	70.08	5.91	70.82	5.98	70.29	5.86	70.44	5.85
Ce-D16(20)-13.0-000	A	41.48	7.96	41.39	7.94	41.41	7.95	41.38	7.91	40.57	8.00
Ce-D16(20)-13.0-033	A	33.88	5.96	33.80	5.90	33.72	5.91	33.70	5.89	30.68	0.92
Ce-D16(20)-24.8-000	A	42.88	5.92	42.73	7.80	43.08	5.98	42.68	5.89	42.83	8.00
Ce-D16(20)-24.8-033	A	33.84	0.98	33.77	0.98	33.84	1.00	33.68	0.96	29.96	0.59
Ce-D16(20)-24.8-066	A	24.39	5.71	23.97	5.74	23.96	5.91	23.66	5.96	22.99	8.00
CeW-D16(20)-13.0-000	A	40.14	6.00	40.02	5.93	40.14	5.93	39.91	5.89	40.53	8.00
CeW-D16(20)-13.0-033	A	33.02	0.97	32.87	0.95	32.95	1.00	33.63	0.99	30.71	0.95
CeW-D16(20)-13.0-066	A	22.54	7.96	22.48	7.96	22.55	5.93	22.38	7.94	22.21	8.00
CeW-D16(20)-24.8-000	A	43.91	5.94	43.70	5.83	43.85	5.98	43.65	5.78	42.97	8.00

CeW-D16(20)-24.8-033	A	31.04	5.90	31.08	6.01	31.09	7.95	31.01	5.78	30.03	8.00
CeW-D16(20)-24.8-066	A	23.19	7.84	23.08	7.83	23.17	7.95	23.10	7.96	23.17	8.00
CeW-D16(20)-25.1-000	A	42.13	5.92	41.05	5.92	41.60	5.98	41.42	5.96	41.16	5.80
CeW-D22(28)-25.1-000	A	79.56	7.60	79.49	7.61	79.84	7.72	79.52	7.66	82.14	8.00
CeW-D22(32)-25.1-000	A	95.06	7.99	91.59	7.82	91.72	7.80	91.35	7.48	92.01	8.00
CeW-D25(32)-25.1-000	A	114.11	6.00	113.16	5.63	113.28	5.98	112.94	5.96	111.04	8.00
CfW-D16(20)-25.1-000-1	A	46.13	7.96	45.99	7.95	46.06	7.96	46.13	7.96	43.99	8.00
CfW-D19(24)-25.1-000	B	62.75	7.97	86.09	5.64	59.35	5.98	64.54	5.86	63.20	6.00
CfW-D22(28)-25.1-000	A	84.69	7.78	84.17	7.72	84.25	7.72	83.88	7.66	85.48	8.00
CfW-D25(32)-25.1-000	A	104.95	7.91	104.85	7.87	104.89	7.91	104.65	7.84	109.56	8.00
CfW-D16(20)-25.1-000-2	A	41.86	5.85	41.56	5.89	42.06	7.96	42.36	6.00	43.57	8.00
CfW-D16(20)-25.1-033	A	32.88	2.02	32.68	1.97	32.92	1.99	33.00	1.96	30.29	1.83
CfW-D16(20)-25.1-066	A	27.93	1.97	27.74	1.87	27.79	1.99	27.46	1.87	26.58	5.76
CfW-D16(28)-25.1-000	B	43.69	5.61	43.99	5.94	42.94	5.86	43.38	7.84	44.33	8.00

4.2 Training accuracy

Fig. 8 shows the training accuracy. The results shown in **Fig. 8** contains 20 % of the training data set described in Section 3.6. The root mean squared error (RMSE) and the coefficient of determination (R^2) are used to examine the accuracy.

$$\text{RMSE} = \sqrt{\frac{1}{N}\sum_{i=1}^{N}(y_i - \hat{y}_i)^2}, \tag{6}$$

$$R^2 = 1 - \frac{\frac{1}{N}\sum_{i=1}^{N}(y_i - \hat{y}_i)^2}{\frac{1}{N}\sum_{i=1}^{N}(y_i - \bar{y}_i)^2}, \tag{7}$$

where y_i and $\hat{y}_i$ are the test and predicted values of the number i, respectively. $\bar{y}_i$ is the average value of y_i.

Four ML models were used, and their R^2 was 0.98 or 0.99. These values are almost identical to those reported in previous studies [14,21]. Moreover, the RMSE of RF, XB, and LG ranged from 0.80 to 0.93; thus, the differences were small. The RMSE of the ANN was 3.24, which was greater than that of the other algorithms.
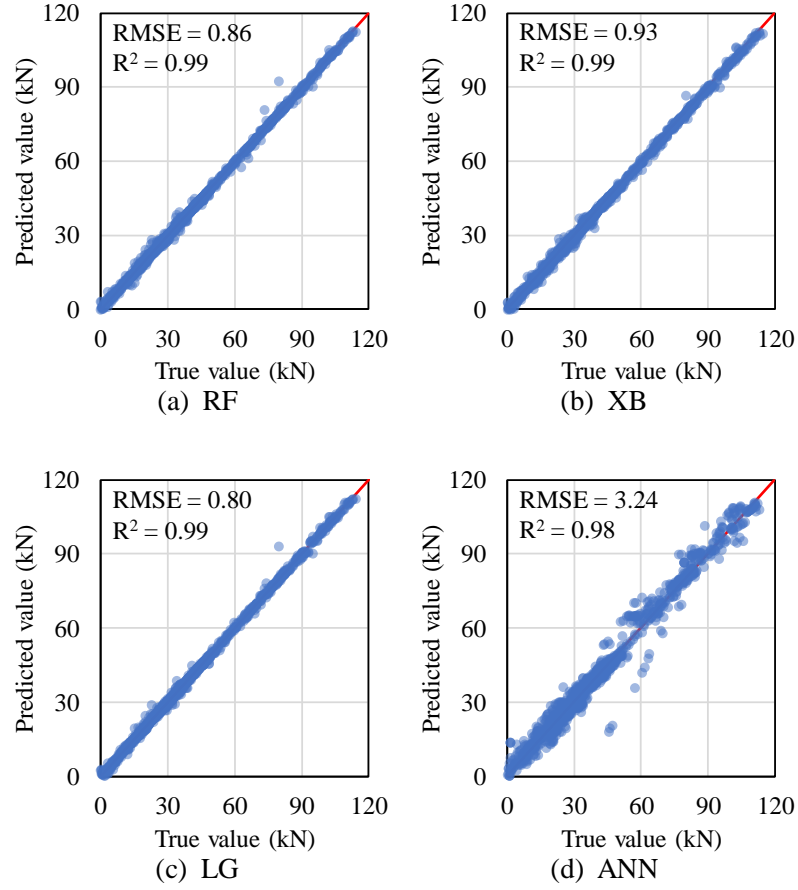
Fig. 8 Training accuracy.

5 DISCUSSION

5.1 *Validation accuracy of Q_{max} and δ_{max}*

The validation accuracies are listed in **Table 4**. The "Pred." column in **Table 4** indicates whether the specimens were used for learning. The specimens of Pred. A were used for this purpose, whereas those of Pred. B were not used. **Figs. 9** and **10** show the relationships between the predicted and tested values for Q_{max} and δ_{max}, respectively. In these figures, the red squares represent the specimens of Pred. B.

The mean absolute error (MAE) was used to examine the validation accuracy.

$$\text{MAE} = \frac{1}{N}\sum_{i=1}^{N}|y_i - \hat{y}_i|. \tag{8}$$

As can be seen in **Fig.9**, most of the maximum shear loads were well predicted by all models. In RF, the accuracy was poor for one specimen. **Table 4** shows that this specimen was CfW-D19(24)-25.1-000. This specimen was classified as a Pred. B; therefore, Q_{max} could not be accurately predicted. Nevertheless, the MAE of RF is smaller than that of the ANN; thus, the prediction accuracy of the decision tree-based algorithm was better than that of the ANN. Subsequently, **Fig. 10** focuses on the comparison of the accuracies of δ_{max}, which were low for all algorithms. In particular, the δ_{max} of Pred. B could hardly be predicted. In addition, as well as Q_{max}, the MAE of the ANN was the worst. From these results, prediction for δ_{max} was difficult.
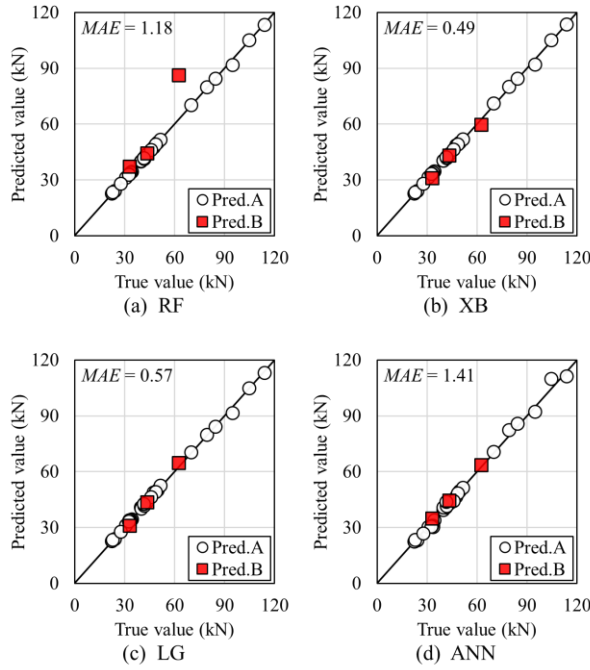

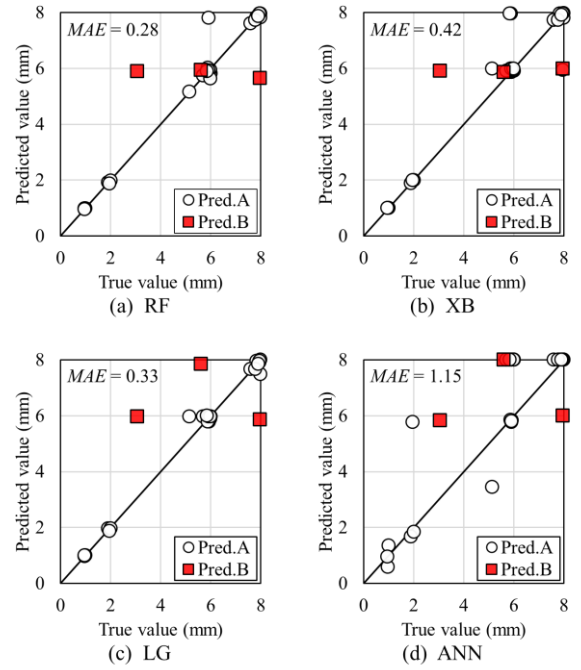**Fig. 9** Validation accuracy of maximum shear load Q_{max}.

Fig. 10 Validation accuracy of shear displacement during maximum shear load δ_{max}.

5.2 *Envelope curve of the test specimens*

In this section, the prediction accuracy of the envelope curves is discussed. **Fig. 11** shows the validation and test results of *the Q–δ* curves. **Tables 5** and **6** list the MAE of each specimen and the average MAE, respectively.

Although cyclic shear loads were applied to the specimens, envelope curves were

used for this investigation. Therefore, the test results waved based on the loading cycles. Focusing on the results of RF, XB, and LG in all figures, the prediction results for Pred. A are in good agreement with the test results. **Tables 5** and **6** show that the range of MAE for the three algorithms is 0.09 to 0.86, and that of the average values of each algorithm is 0.22–0.39.

The prediction results of the Pred. B are shown in Figs. **11** (c), (z) and (af); the prediction accuracies were not good as the range of MAE was from 1.22 to 22.55, and the average RF for Pred. B was 9.04, which is 41 times greater than 0.22, the average RF for Pred. A. In the decision tree-based algorithm, the prediction output is selected from the learning data, and it is difficult to make predictions for parameters that were not used in the training data.

However, the behavior of the ANN was not as good as that of the other algorithms. Nevertheless, the ANN can accurately predict the test results of both Pred. A and Pred. B, and The MAEs of both predictions were 0.78–5.37 and 1.21–2.47, respectively. Additionally, the average values of both predictions were 1.63 and 1.97, respectively; thus, there is no significant difference observed. For an ANN, the output does not always match the training data because it is obtained from complex calculations based on neurons. Therefore, the ANN can make good predictions for unknown parameters.
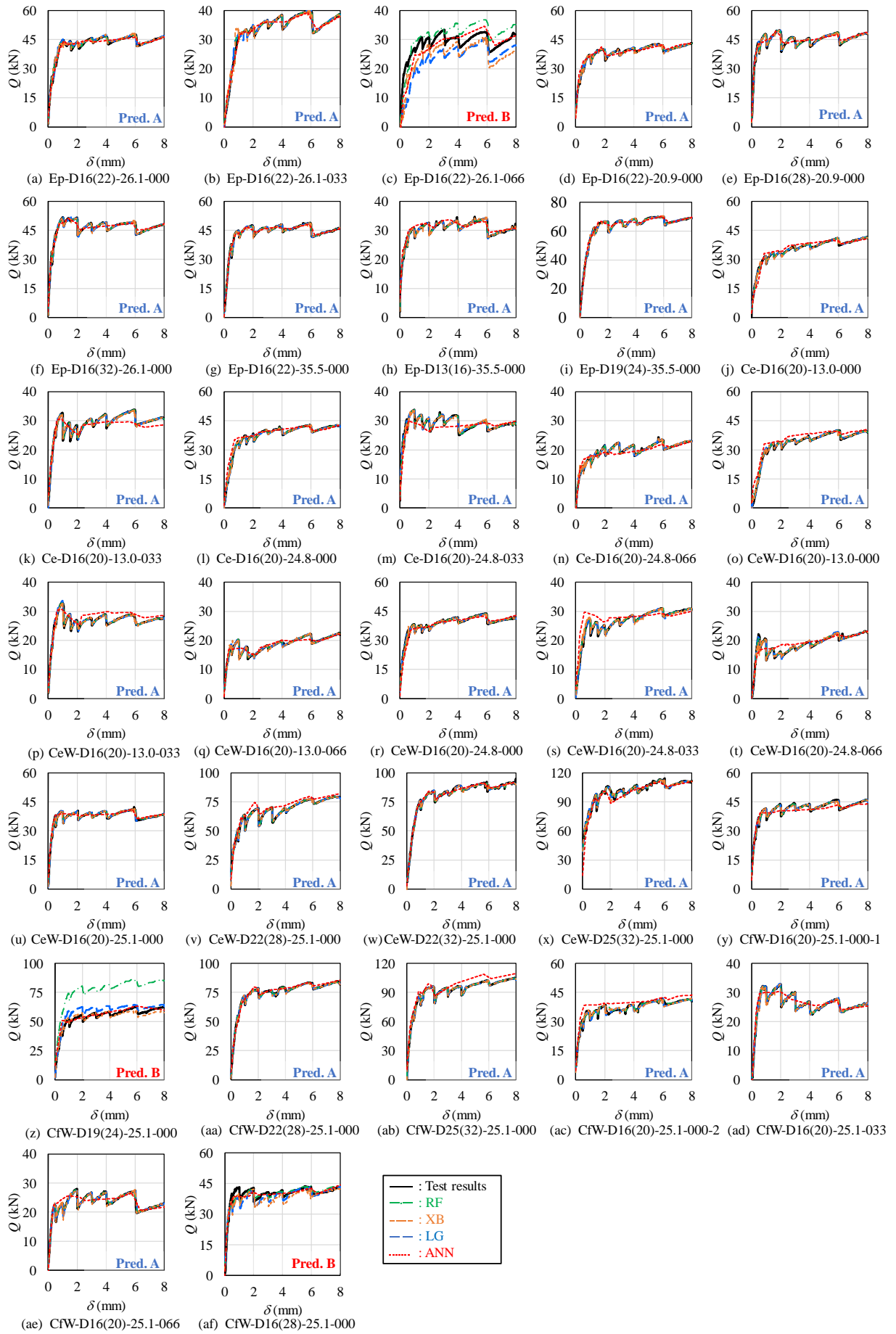
Fig. 11 Envelope curves of validation results.

Table 5
MAE (kN) of the validation results.

Specimen ID	Pred.	RF	XB	LG	ANN
Ep-D16(22)-26.1-000	A	0.44	0.56	0.51	1.03
Ep-D16(22)-26.1-033	A	0.34	0.53	0.42	0.89
Ep-D16(22)-26.1-066	B	3.35	4.30	5.20	2.47
Ep-D16(22)-20.9-000	A	0.15	0.30	0.22	1.05
Ep-D16(28)-20.9-000	A	0.18	0.31	0.24	1.26
Ep-D16(32)-20.9-000	A	0.15	0.25	0.21	1.00
Ep-D16(22)-35.5-000	A	0.13	0.26	0.21	0.78
Ep-D13(16)-35.5-000	A	0.12	0.23	0.18	0.98
Ep-D19(24)-35.5-000	A	0.18	0.38	0.24	1.05
Ce-D16(20)-13.0-000	A	0.15	0.27	0.21	1.31
Ce-D16(20)-13.0-033	A	0.16	0.33	0.24	1.74
Ce-D16(20)-24.8-000	A	0.14	0.31	0.20	1.29
Ce-D16(20)-24.8-033	A	0.25	0.53	0.25	1.82
Ce-D16(20)-24.8-066	A	0.13	0.24	0.19	1.10
CeW-D16(20)-13.0-000	A	0.26	0.34	0.32	2.31
CeW-D16(20)-13.0-033	A	0.18	0.29	0.22	1.72
CeW-D16(20)-13.0-066	A	0.09	0.23	0.18	0.79
CeW-D16(20)-24.8-000	A	0.18	0.39	0.23	1.15
CeW-D16(20)-24.8-033	A	0.17	0.42	0.22	2.03
CeW-D16(20)-24.8-066	A	0.19	0.35	0.22	1.19
CeW-D16(20)-25.1-000	A	0.20	0.31	0.20	0.88
CeW-D22(28)-25.1-000	A	0.21	0.48	0.37	3.72
CeW-D22(32)-25.1-000	A	0.37	0.50	0.46	1.23
CeW-D25(32)-25.1-000	A	0.51	0.86	0.70	3.32
CfW-D16(20)-25.1-000-1	A	0.24	0.36	0.26	1.49
CfW-D19(24)-25.1-000	B	22.55	1.82	4.25	2.23
CfW-D22(28)-25.1-000	A	0.23	0.43	0.38	1.51
CfW-D25(32)-25.1-000	A	0.20	0.36	0.35	5.37
CfW-D16(20)-25.1-000-2	A	0.48	0.63	0.54	2.76
CfW-D16(20)-25.1-033	A	0.15	0.29	0.22	1.24
CfW-D16(20)-25.1-066	A	0.21	0.29	0.28	1.26
CfW-D16(28)-25.1-000	B	1.22	1.99	1.64	1.21

Table 6
Average values of MAE for each classification.

Classification	RF	XB	LG	ANN
pred. A	0.22	0.38	0.29	1.63
pred. B	9.04	2.70	3.70	1.97
Epoxy adhesive anchors	0.56	0.79	0.83	1.17
Cement based anchors	1.24	0.52	0.53	1.85
All anchors	1.05	0.60	0.61	1.66

5.3 *Prediction results of the parametric analysis*

In this section, the authors perform a parametric analysis using f_c, r_φ, *and* r_N. **Table 7** and **Fig. 12** show the conditions of the parametric analysis and the prediction results of the four algorithms, respectively. f_c, r_φ, r_N are set to 10–40, 1.0–2.2, and 0.20–0.80, respectively. The other parameters are set to values that are within the training data and different from the training data.

Table 7
Conditions of parametric analysis.

ID	f_c	f_g	A_s	r_φ	f_y	τ_a	r_N
Sm-fc10	10	65	198.6	1.375	400	25	0.00
Sm-fc20	20	65	198.6	1.375	400	25	0.00
Sm-fc30	30	65	198.6	1.375	400	25	0.00
Sm-fc40	40	65	198.6	1.375	400	25	0.00
Sm-r$_a$10	24	65	198.6	1.0	400	25	0.00
Sm-τ_a14	24	65	198.6	1.4	400	25	0.00
Sm-τ_a18	24	65	198.6	1.8	400	25	0.00
Sm-τ_a22	24	65	198.6	2.2	400	25	0.00
Sm-r$_N$02	24	65	198.6	1.375	400	25	0.20
Sm-r$_N$033	24	65	198.6	1.375	400	25	0.33
Sm-r$_N$04	24	65	198.6	1.375	400	25	0.40
Sm-r$_N$06	24	65	198.6	1.375	400	25	0.66
Sm-r$_N$066	24	65	198.6	1.375	400	25	0.20
Sm-r$_N$08	24	65	198.6	1.375	400	25	0.80

(a) Sm-fc
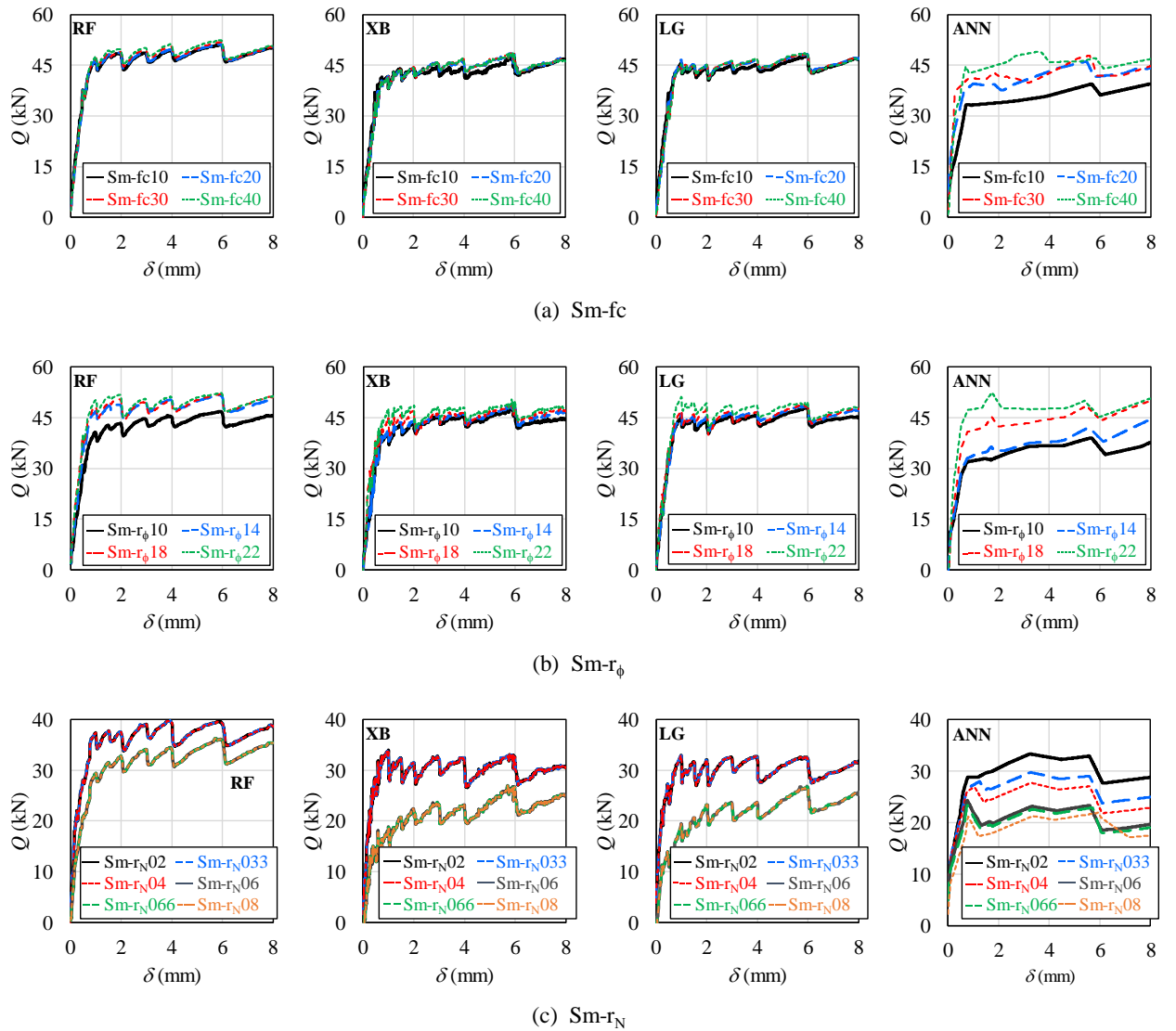
(b) Sm-r$_\phi$

(c) Sm-r$_N$

Fig. 12 Prediction results of the parametric analysis.

As shown in **Fig. 12** (a), the prediction results of RF, XB, and LG were almost iden-

tical, although f_c was different. However, The ANN showed different behavior depending on the degree of f_c. In the training data, although f_c was set to 13.0–35.5 N/mm², the amount of data was considered insufficient. Therefore, the mechanical behaviors were almost the same when the decision tree-based algorithm was used. However, the ANN could predict the behavior by considering the difference in f_c.

Fig. 12 (b) shows that in the prediction results of RF, XB, and LG, when r_φ is larger, Q is slightly larger. For the ANN, with r_φ is larger, Q is significantly larger. Finally, **Fig. 12** (c) is focused on. The results of RF, XB, and LG are classified into two values, whereas the ANN can predict the behavior based on r_N. In the training data, r_N was only set to 0.33 and 0.66; therefore, the results of RF, XB, and LG were classified into two patterns. As mentioned earlier, when the parameters are close to the training data, RF, XB, and LG can predict the mechanical behavior well. However, when they are not close to the training data, these algorithms do not predict the behavior well. Therefore, ANN is useful for predicting dowel action when the training data are limited.

6 CONCLUSION

In this study, the shear loading test results of post-installed anchors were predicted using RF, XB, LG, and ANN. The 32 test results were used. The values for f_c and d_d were set at 13.0-35.5 N/mm² and 13-25 mm, respectively, and epoxy and cement-based adhesives were applied. The findings of this study are as follows:

1) The training accuracies of the four algorithms agreed well with test results, because R^2 = 0.98 or 0.99. In addition, Q_{max} could be well estimated by the four algorithms; however, some δ_{max} values could not be reasonably estimated.

2) The decision tree-based algorithms accurately predicted the Q–δ curves, which were used for the training data (the specimens of Pred. A). The waved behavior based on

the loading cycle was also tracked by using these algorithms. However, the prediction accuracy was lower for specimens that were not used for the training data (the specimens of Pred. B).

3) When the ANN was used, although the ANN could reasonably predict the test results for Pred. A, MAE was bigger than that of RF, XB, and LG. However, the test results for Pred. B can also be accurately predicted. No significant difference was found in the average MAE between Pred. A and Pred. B.

4) Parametric analysis was performed using the parameters f_c, r_φ, and r_N. When RF, XB, and LG, were used, the Q–δ curves did not differ in some cases, although the parametric values varied. However, when the ANN was used, the Q–δ curves differed as a function of the parameters. Therefore, when the training data are limited, the ANN is useful for predicting the dowel action of the post-installed anchors.

To consider the shear displacement on structural designs, a mechanical model must be estimated; hence, for estimating mechanical behaviors of post-installed anchors, a complex modelling [25-27] or finite element analysis [37] were required. However, according to the result of this study, the mechanical behaviors could be easily estimated using ANN. In addition, future studies will focus on predicting cyclic behavior and other failure modes; for instance, concrete break failure.

References

[1] ACI 318–14. Building code requirements for structural concrete. Am Conc Inst, Farmington Hill, Michigan, 2014.

[2] AISC 360–16. Specifications for structural steel buildings. Am Inst Steel Const, Chicago, Illinois, 2019

[3] ETAG 001, Metal anchors for use in concrete, Part 5 Bonded anchors. Euro Org Tech Asses, Brussels, Belgium, 2012.

[4] EOTA TR069, Design method for anchorage of post–installed reinforcing bars(rebars) with improved bond–splitting behavior as compared to EN 1992–1–1. Euro Org Tech Asses, Brussels, Belgium, 2019.

[5] JBDPA. Eternal seismic retrofitting manual for existing reinforced concrete building. Japan Build Disast Prev Assoc, Minato, Tokyo, 2002.

[6] Friberg BF. Design of dowels in the transverse joints of concrete pavements. Proc Am Soc Civ Eng 1938;64(9):1809–28.

[7] Vintzēleou EN, Tassios TP. Mathematical models for dowel action under monotonic and cyclic conditions, Mag Conc Res 1986;38(134):13–22. (https://doi.org/10.1680/macr.1986.38.134.13)

[8] Sorensen JH, Hoang LC, Olesen JF, Fischer G. Testing and modeling dowel and catenary action in rebars crossing shear joints in RC. Eng Struct 2017;145:234–45. (https://doi.org/10.1016/j.engstruct.2017.05.020)

[9] Ghayeb HH, Razak HA, Sulong NHR. Performance of dowel beam–to–column connections for precast concrete systems under seismic loads: A review, Const Build Mater 2020;237:117582. (https://doi.org/10.1016/j.conbuildmat.2019.117582)

[10] Alhaidary H, Al–Tamimi AK. Importance of performance certification for post–installed anchors: an experimental assessment. Struct 2021;29:273–85. (https://doi.org/10.1016/j.istruc.2020.11.005)

[11] Mahrenholtz C, Eligehausen R, Reinhardt H. Design of post–installed reinforcing bars as end anchorage or as bonded anchor. Eng Struct 2015;100:645–55. (https://doi.org/10.1016/j.engstruct.2015.06.028)

[12] Ma X, Sha J, Wang D, Yu Y, Yang Q, Niu X. Study on a prediction of P2P network

loan default based on the machine learning LightGBM and XGboost algorithms according to different high dimensional data cleaning. Elect Com Res Appl 2018;31:24-39. (https://doi.org/10.1016/j.elerap.2018.08.002)

[13] Fan J, Wang X, Wu L, Zhou H, Zhang F, Yu X, Lu X, Xiang Y. Comparison of support vector machine and extreme gradient boosting for predicting daily global solar radiation using temperature and precipitation in humid subtropical climates: A case study in China. Ener Conve Manag 2018;164:102-11. (https://doi.org/10.1016/j.enconman.2018.02.087)

[14] Chen C, Zhang Q, Mac Q, Yu B. LightGBM-PPI: Predicting protein-protein interactions through LightGBM with multi-information fusion. Chem Intel Labo Syst 2019;191:54-64. (https://doi.org/10.1016/j.chemolab.2019.06.003)

[15] Alabdullah AA, Iqbal M, Zahid M, Khan K, Amin MN, Jalal FE. Prediction of rapid chloride penetration resistance of metakaolin based high strength concrete using light GBM and XGBoost models by incorporating SHAP analysis. Const Build Mater 2022;345:128296. (https://doi.org/10.1016/j.conbuildmat.2022.128296)

[16] Demir F. Prediction of elastic modulus of normal and high strength concrete by artificial neural networks. Const Build Mater 2008;22:1428-35. (https://doi.org/10.1016/j.conbuildmat.2007.04.004)

[17] Yan K, Shi C. Prediction of elastic modulus of normal l and high strength concrete by support vector machine. Const Build Mater 2010;24:1479-85. (https://doi.org/10.1016/j.conbuildmat.2010.01.006)

[18] Nehdi ML, Soliman AM. Artificial intelligence model for early-age autogenous shrinkage of concrete, ACI Mater J 2012;109 (3):353–62.

[19] Liu J, Yan K, Zhao X, Hu Y. Prediction of autogenous shrinkage of concretes by support vector machine. Int J Pavem Res Tech 2016;9:169–77. (https://doi.org/10.1016/j.ijprt.2016.06.003)

[20] Kang MC, Yoo DY, Gupta R. Machine learning-based prediction for compressive and flexural strengths of steel fiber-reinforced concrete. Const Build Mater 2021;266:121117. (https://doi.org/10.1016/j.conbuildmat.2020.121117)

[21] Su M, Zhong Q, Peng H, Li S. Selected machine learning approaches for predicting the interfacial bond strength between FRPs and concrete. Const Build Mater 2021;270:121456. (https://doi.org/10.1016/j.conbuildmat.2020.121456)

[22] Spyridis P, Olalusi OB. Predictive Modelling for concrete failure at anchorages using machine learning techniques. Mater 2021;14:62. (https://doi.org/10.3390/ma14010062)

[23] Olalusi OB, Panagiotis S. Machine learning-based models for the concrete breakout capacity prediction of single anchors in shear, Advan Eng Soft 2020; 147;102832. (https://doi.org/10.1016/j.advengsoft.2020.102832)

[24] Olalusi OB, Awoyera PO. Shear capacity prediction of slender reinforced concrete structures with steel fibers using machine learning. Eng Struct 2021;227:111470. (https://doi.org/10.1016/j.engstruct.2020.111470)

[25] Takase Y. Testing and modeling of dowel action for a post–installed anchor subjected to combined shear and tensile forces. Eng Struct 2019;195:551–8. (https://doi.org/10.1016/j.engstruct.2019.05.086)

[26] Matsunaga K, Takase Y, Abe T. Modeling of dowel action for cast–in and post–installed anchors considering bond property. Eng Struct 2021;245:112773. (https://doi.org/10.1016/j.engstruct.2021.112773)

[27] Matsunaga K, Takase Y, Abe T, Orita G, Ando S. Property of cement based adhesive anchor constructed below zero and estimation of mechanical behavior. J Struct Const Eng 2022;87(796):556-66. (in Japanese) (https://doi.org/10.3130/aijs.87.556)

[28] Takase Y, Abe T, Orita G, Ando S. Anchorage Property of cement-based adhesive anchor with frost resist acceleration for cold weather construction. Conc J 2022;60(6):525-32. (in Japanese)

[29] Japan Construction Anchor Assessment. https://www.anchor-jcaa.or.jp/certification/system.html (2022.8.23 accessed)

[30] Japanese Industrial Standards: JIS 1108, Method of test for compressive strength of concrete, 2018.

[31] Japanese Industrial Standards: JIS Z 2241, Metallic materials – Tensile testing –

Method of test at room temperature, 2011.

[32] Japanese Industrial Standards: JIS G 3112, Steel bars for concrete reinforcement, 2010.

[33] Breiman L: Random Forests, Mach Learn 2001;45(1):5-32. (https://doi.org/10.1023/A:1010933404324)

[34] Chen T, Guestrin C. XGBoost: a scalable tree boosting system. Proc of 22nd ACM SIGKDD Int Conf Know Disco Data Min 2016;785-94.

[35] Ke G, Meng Q, Finley T, Wang T, Chen W, Ma W, Ye Q, Liu TY. LightGBM: a highly efficient gradient boosting decision tree. 31st Conf Neu Info Proce Syst NIPS 2017;3146-54.

[36] Krishna BM, Reddy VGP, Shafee M, Tadepalli T. Condition assessment of RC beams using artificial neural networks. Struct 2020;23:1-12. (https://doi.org/10.1016/j.istruc.2019.09.014)

[37] Ishida Y, Sakata H, Takase Y, Maida Y, Shirai Y, Sato T. FEM Analysis of Post-installed anchors under combined stress. Comput Model Conc Struct 2018;963-72. (http://dx.doi.org/10.1201/9781315182964-111)